

Simulation of a non-equilibrium helium plasma bullet emerging into oxygen at high pressure (250–760 Torr) and interacting with a substrate

Wen Yan^{1,2} and Demetre J. Economou^{2,a)}

¹*School of Physics and Materials Engineering, Dalian Nationalities University, Dalian 116600, People's Republic of China*

²*Plasma Processing Laboratory, Department of Chemical and Biomolecular Engineering, University of Houston, Houston, Texas 77204, USA*

(Received 16 June 2016; accepted 6 September 2016; published online 27 September 2016)

A two-dimensional computational study of a plasma bullet emanating from a helium gas jet in oxygen ambient at high pressure (250–760 Torr) was performed, with emphasis on the bullet interaction with a substrate. Power was applied in the form of a trapezoidal +5 kV pulse lasting 150 ns. A neutral gas transport model was employed to predict the concentration distributions of helium and oxygen in the system. These were then used in a plasma dynamics model to investigate the characteristics of the plasma bullet during its propagation and interaction with a substrate. Upon ignition, the discharge first propagated as a surface wave along the inner wall of the containing tube, and then exited the tube with a well-defined ionization front (streamer or plasma bullet). The plasma bullet evolved from a hollow (donut-shaped) feature to one where the maximum of ionization was on axis. The bullet propagated in the gap between the tube exit and the substrate with an average speed of $\sim 2 \times 10^5$ m/s. Upon encountering a metal substrate, the bullet formed a conductive channel to the substrate. Upon encountering a dielectric substrate, the bullet turned into an ionization wave propagating radially along the substrate surface. For a conductive substrate, the radial species fluxes to the surface peaked on the symmetry axis. For a dielectric substrate, a ring-shaped flux distribution was observed. The “footprint” of plasma-surface interaction increased either by decreasing the gap between tube exit and substrate, decreasing the relative permittivity of an insulating substrate, or decreasing pressure. As the system pressure was lowered from 760 to 250 Torr, the discharge was initiated earlier, and the plasma bullet propagation speed increased. A reverse electric field developed during the late stages of the ramp-down of the pulse, which accelerated electrons forming a brief backward discharge. *Published by AIP Publishing.*

[<http://dx.doi.org/10.1063/1.4963115>]

I. INTRODUCTION

Non-thermal (cold) high pressure (notably 1 atm) plasmas are investigated intensely because of current and future applications ranging from surface modification and materials processing to plasma medicine.^{1–6} Various types of non-thermal plasma sources have been developed and studied.^{7,8} In particular, cold atmospheric pressure plasma jets (APPJ) have attracted considerable attention, compared to other plasmas in confined geometries, primarily due to their ability to deliver various active species to relatively remote locations for localized treatment.

Understanding the physical and chemical processes taking place in the plasma jet is critically important. To this end, numerous experimental and simulation studies have contributed to a better understanding of these systems. For example, it was demonstrated that the plasma jet is typically composed of streamers or “plasma bullets” propagating at supersonic speeds (10^4 – 10^5 m/s).^{9,10} Images revealed that the bullet is in fact hollow, having a donut-shaped structure.^{11,12} Plasma diagnostics showed that the streamer dynamics depends on electron temperature.¹³ Using two-photon

laser-induced fluorescence spectroscopy, the O number density in a plasma jet emerging in 1 atm air ambient was found to reach $5.8 \times 10^{15} \text{ cm}^{-3}$.¹⁴

Experimental measurements have been complemented by modeling and simulation. Several research groups have developed two-dimensional (2-D) axisymmetric models to explain the experimental observations. Using the local field approximation, Naidis^{15,16} successfully simulated the donut-shaped plasma bullet and showed that the formation of such structure is due to radial non-uniformity of the electron impact ionization rate of the gas species. The computational studies by Breden *et al.*^{17,18} and Norberg *et al.*¹⁹ provided valuable insights into the dynamics of plasma bullet propagation and its interaction with surfaces.

Plasma jets can be generated in different gases using different means of electrical excitation. A typical plasma jet consists of a dielectric tube through which a jet of noble gas exhausts into an ambient gas. High voltage (HV) nanosecond pulse waveforms are applied to a ring electrode wrapped around the tube to form a plasma jet.¹⁰ The gas is near room temperature, making these devices ideal for the treatment of thermosensitive materials (e.g., human skin).

Previous experimental studies by Xian *et al.*²⁰ and Schmidt-Bleker *et al.*²¹ investigated He plasma jets and the

^{a)}E-mail: economou@uh.edu

resulting bullets propagating in oxygen ambient. Xian *et al.*²⁰ observed that the plasma jet became shorter and thinner by increasing the mole fraction of O₂ in the ambient gas. Winter *et al.*²² found a drastic decrease in the measured metastable He density by decreasing the mole fraction of oxygen in the ambient gas. Several simulations^{23–25} were performed to investigate the generation mechanism of reactive oxygen species in discharges fed by He/O₂ mixtures. Schmidt-Bleker *et al.*²¹ investigated, by a combination of simulation and experiment, the influence of electronegativity of the ambient gas on the propagation of the plasma bullet. Despite the plethora of investigations, however, several aspects of the effect of substrate conductivity and system pressure on the plasma jet and its interaction with surfaces have not been elucidated.

In this work, a two dimensional axisymmetric fluid model was developed to investigate the discharge dynamics of a helium high pressure plasma jet emerging in oxygen ambient. Physical processes including discharge ignition and propagation inside the tube, plasma bullet propagation in the open gap, and its interaction with a substrate were studied. Particular emphasis was placed on the effect of the conductivity of the substrate surface (conductor vs. insulator) and system pressure (250–760 Torr).

II. MODEL DEVELOPMENT

The plasma jet configuration studied in this work is shown in Fig. 1. The overall problem was divided into two parts: a neutral gas flow model and a plasma dynamics model. Fig. 1(a) shows the simulation domain; only the right half of the axisymmetric (r, z) system is shown. The larger domain (ADEG) was used for the neutral gas model, while the smaller domain (ACFG) was used for the plasma dynamics model. A detail of the plasma region is shown in Fig. 1(b). Helium gas flowed through a dielectric tube (relative permittivity of 4) with 2 mm ID (inner diameter). A high voltage (HV) ring electrode (1.5 mm long with 4 mm ID and 4.4 mm OD (outer diameter)) was embedded in the dielectric wall, similar to the works by Raja *et al.*^{17,18} and Lu *et al.*²⁶ The distance between the downstream edge of the HV electrode and the tube exit was 3.5 mm.

A trapezoidal voltage pulse with amplitude of +5 kV was applied to the ring electrode, see Fig. 1(c). The rise and

fall time of the voltage was 10 ns each. Thus, the voltage on the electrode was steady at 5 kV for 130 ns. Following common practice,^{15,18,19} only a single pulse was simulated. This implies that the pulse OFF time interval is long enough (\sim gas residence time) for the system volume to be replenished with fresh gas before the next voltage pulse is applied. The substrate was placed 5 mm away from the tube exit perpendicular to the jet axis. Both conductive and insulating substrates were examined. In the case of insulator (relative permittivity either 5 or 15), the thickness of the dielectric layer facing the plasma was 0.5 mm. This layer was on top of a grounded metal wall.

A. Neutral gas flow model

The helium working gas flowed through the dielectric tube and emerged into an oxygen ambient. The average gas flow velocity in the tube was 5 m/s (at 760 Torr), corresponding to a Reynolds number of 86, implying laminar flow. The neutral gas flow model consisted of the total mass continuity equation (Eq. (1)), the momentum conservation (Navier-Stokes) equations (Eq. (2)), and the species mass balance equation (Eq. (3))

$$\nabla \cdot (\rho \mathbf{u}) = 0, \quad (1)$$

$$(\nabla \cdot \rho \mathbf{u} \mathbf{u}) = -\nabla p - (\nabla \cdot \boldsymbol{\tau}) + \mathbf{F}, \quad (2)$$

$$\nabla \cdot (\rho w_i \mathbf{u}) + \nabla \cdot \mathbf{J}_i = 0. \quad (3)$$

Here \mathbf{u} is the mass-average velocity of the mixture, ρ is the mixture density (helium = 0.1625 kg m⁻³, oxygen = 1.284 kg m⁻³ at 760 Torr), $\boldsymbol{\tau}$ is the stress tensor for a Newtonian fluid, and \mathbf{F} is the body force. w_i and \mathbf{J}_i are mass fraction and diffusion flux of species i , respectively. For laminar flow, $\mathbf{J}_i = -\rho D_i \nabla w_i$, where D is the (molecular) diffusion coefficient (helium in oxygen = 7.2 × 10⁻⁵ m² s⁻¹ at 760 Torr (Ref. 26)). The effect of the plasma on the neutral gas flow was not considered in this work. An indication of the weak interaction between neutral gas flow and plasma under the present conditions is the fact that the temperature of the fluid in the jet hardly increases above ambient.^{18,27,28} The boundary conditions are summarized in Table I, with the corresponding boundaries shown in Fig. 1(a). The velocity of the entrained oxygen ambient gas was set at 0.3 m/s (at 760 Torr)

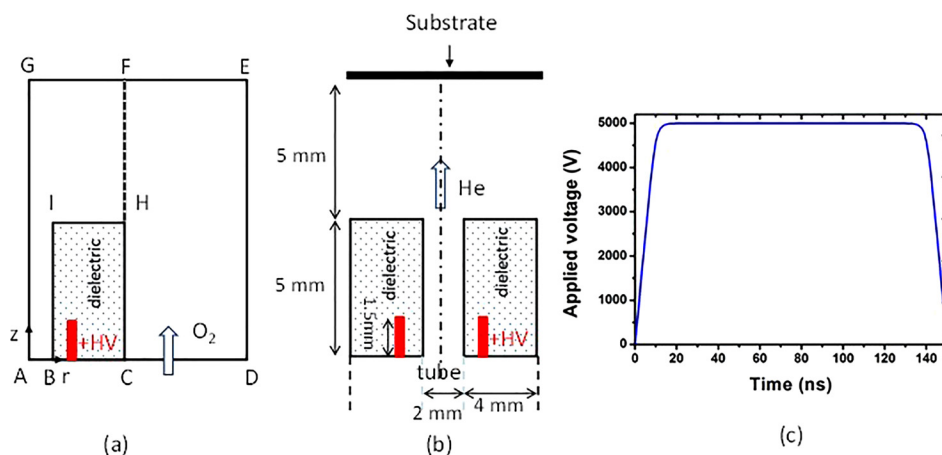


FIG. 1. Plasma jet configuration studied: (a) Computational domain; due to axisymmetric (r, z) nature of the problem, only half of the domain is shown. The axis of symmetry is AG. Helium is fed through boundary AB (1 mm radius), while O₂ enters through annular boundary CD. (b) Detail of the plasma region, not showing the region of injection of the ambient oxygen gas. (c) Applied voltage.

TABLE I. Boundary conditions for the neutral gas model. Boundaries AB, CD, etc., are shown in Fig. 1(a). u_z and u_r are the velocity components in the axial and radial direction, respectively. \mathbf{n} is the unit normal vector pointing towards the boundary. Values of u_z are at 760 Torr, and scale inversely proportionally to pressure.

	AB	CD	DE	EG	BIHC
u_z	5 m/s	0.3 m/s	0	0	0
u_r	0	0	$\frac{\partial u_r}{\partial r} - \frac{1}{3}(\nabla \cdot \mathbf{u}) = 0^a$	0	0
w_{He}	1	0	$\frac{\partial w_{He}}{\partial r} = 0$	$\frac{\partial w_{He}}{\partial z} = 0$	$\nabla w_{He} \cdot \mathbf{n} = 0$
w_{O_2}	0	1	$\frac{\partial w_{O_2}}{\partial r} = 0$	$\frac{\partial w_{O_2}}{\partial z} = 0$	$\nabla w_{O_2} \cdot \mathbf{n} = 0$

^aCorresponds to zero stress.

on face CD in Fig. 1(a).²⁹ The governing Equations (1)–(3) were solved using a steady-state solver in COMSOL.³⁰

B. Plasma dynamics model

Plasma dynamics was governed by a fluid model, which is based on the continuity Eq. (4), with the drift-diffusion approximation Eq. (5), the electron energy conservation Eq. (6) and Poisson's Eq. (7)^{31,32}

$$\frac{\partial n_i}{\partial t} + \nabla \cdot \Gamma_i = \sum_j R_{ij}, \quad (4)$$

$$\Gamma_i = \text{sgn}(q_i) n_i \mu_i \mathbf{E} - D_i \nabla n_i + \mathbf{u} n_i, \quad (5)$$

$$\begin{aligned} \frac{\partial (n_e)}{\partial t} + \nabla \cdot \left(\frac{5}{3} \mu_e \mathbf{E} n_e - \frac{5}{3} D_e \nabla n_e \right) \\ = -e \Gamma_e \cdot \mathbf{E} - \sum_j \Delta E_j R_{inel,j} - 3 \frac{m_e}{M} k_b n_e \nu_{en} (T_e - T_g), \end{aligned} \quad (6)$$

$$\epsilon_0 \nabla \cdot (\epsilon_r \nabla \Phi) = - \sum_i q_i n_i, \quad (7)$$

where subscripts i and e indicate the i th species and electrons, respectively. n_i is the species density, Γ_i is the flux (in the drift-diffusion approximation), R_{ij} is the rate of production or consumption of species i in reaction j , q_i is the charge of species i ; μ and D are mobility and diffusion coefficient, respectively. $\text{sgn}(q_i)$ is the sign function (positive or negative), \mathbf{E} is the electric field, and Φ is the electric potential. $n_e = n_e \bar{e}$ is the electron energy density and $T_e = \frac{2}{3} \bar{e}$ is the electron equivalent temperature. ΔE and R_{inel} are the energy loss during inelastic collisions and the corresponding reaction rate, respectively. m_e , M , ν_{en} and T_g are the electron mass, gas species mass, electron-neutral momentum transfer collision frequency, and gas temperature, respectively. The right-hand side of the electron energy Eq. (6) consists of three source terms in the order shown: Joule heating and inelastic and elastic collisional energy exchange, respectively. Moreover, in Eq. (7), ϵ_r is the relative permittivity of the dielectric and ϵ_0 is the vacuum permittivity. Table II summarizes the boundary conditions of the plasma dynamics model. The boundary conditions for the particle flux and the electron energy density on solid walls were

TABLE II. Boundary conditions of the plasma dynamics model. Boundaries AG, AB, etc., are shown in Fig. 1(a). “Ring” is the high voltage electrode. Φ_a is the applied voltage.

	AG	AB	BC	CH	HF	GF	BIH	Ring
n_e	$\frac{\partial n_e}{\partial r} = 0$	$\frac{\partial n_e}{\partial z} = 0$	$\frac{\partial n_e}{\partial r} = 0$	Eq. (8)	Eq. (8)	...
n_i	$\frac{\partial n_i}{\partial r} = 0$	$\frac{\partial n_i}{\partial z} = 0$	$\frac{\partial n_i}{\partial r} = 0$	Eq. (9)	Eq. (9)	...
n_m	$\frac{\partial n_m}{\partial r} = 0$	$\frac{\partial n_m}{\partial z} = 0$	$\frac{\partial n_m}{\partial r} = 0$	Eq. (10)	Eq. (10)	...
n_e	$\frac{\partial n_e}{\partial r} = 0$	$\frac{\partial n_e}{\partial z} = 0$	$\frac{\partial n_e}{\partial r} = 0$	Eq. (11)	Eq. (11)	...
Φ	$\frac{\partial \Phi}{\partial r} = 0$	$\frac{\partial \Phi}{\partial z} = 0$	$\frac{\partial \Phi}{\partial z} = 0$	0	0	0	Eq. (13)	Φ_a

$$\Gamma_e \cdot \mathbf{n} = \frac{1}{4} n_e \sqrt{\frac{8k_b T_e}{\pi m_e}} - \alpha_s \sum_i \gamma_i (\Gamma_i \cdot \mathbf{n}) + \alpha'_s \mu_e n_e \mathbf{E}, \quad (8)$$

$$\Gamma_i \cdot \mathbf{n} = \frac{1}{4} n_i \sqrt{\frac{8k_b T_i}{\pi m_i}} + \alpha_s \mu_i n_i \mathbf{E}, \quad (9)$$

$$\Gamma_m \cdot \mathbf{n} = \frac{2\gamma_m}{2 - \gamma_m} \frac{1}{4} n_m \sqrt{\frac{8k_b T_g}{\pi m_m}}, \quad (10)$$

$$\Gamma_e \cdot \mathbf{n} = \frac{1}{2} n_e \sqrt{\frac{8k_b T_e}{\pi m_e}} - \alpha_s 2k_b T_e \sum_i \gamma_i (\Gamma_i \cdot \mathbf{n}), \quad (11)$$

where subscripts e , i , m and ϵ indicate electrons, ions, metastables and electron energy, respectively. \mathbf{n} is the unit normal vector pointing towards the surface, $\gamma_i = 0.01$ is the secondary electron emission coefficient by ion impact, and γ_m is the wall reaction probability of neutral species m . T_i and T_g are the ion and background gas temperature, respectively, taken as $T_i = T_g = 300$ K; k_b is the Boltzmann constant, and α_s and α'_s are switching functions depending on the dot product of \mathbf{E} and \mathbf{n}

$$\alpha_s = \begin{cases} 1 (\mathbf{E} \cdot \mathbf{n} \geq 0) \\ 0 (\mathbf{E} \cdot \mathbf{n} < 0), \end{cases} \quad \alpha'_s = \begin{cases} 0 (\mathbf{E} \cdot \mathbf{n} \geq 0) \\ 1 (\mathbf{E} \cdot \mathbf{n} < 0). \end{cases} \quad (12)$$

The potential at the surface of a dielectric was calculated according to Gauss's law

$$(\mathbf{D}_2 - \mathbf{D}_1) \cdot \mathbf{n} = \sigma_s, \quad \frac{d\sigma_s}{dt} = \mathbf{J}_i \cdot \mathbf{n} + \mathbf{J}_e \cdot \mathbf{n}, \quad (13)$$

where \mathbf{D}_1 and \mathbf{D}_2 are the electric displacement vectors, σ_s is the net charge density accumulated on the dielectric surface, and $\mathbf{J}_e \cdot \mathbf{n}$ and $\mathbf{J}_i \cdot \mathbf{n}$ are the normal components of the electron current density and total ion current density on the surface, respectively. In the case of conductive substrate, the potential of the substrate was set to ground (i.e., zero).

A simplified chemistry mechanism^{15,33} was used in this investigation, which involved reactions in the gas phase as well as recombination and quenching reactions on solid surfaces. The species considered in the model were He, metastable $\text{He}^* = \text{He}(2^3S_1)$, excimer $\text{He}_2^* = \text{He}_2(\alpha^3\Sigma_u)$, He^+ , He_2^+ , O_2 , O , O_2^- , O_2^+ , and electrons. The gas phase reaction mechanism is shown in Table III. For reactions involving

TABLE III. Reactions included in the model. Reaction rate coefficients were described by an Arrhenius form $k = AT^B \exp(-C/T)$. For electron impact reactions, T is the electron temperature in eV, and for reaction between heavy species, T is the gas temperature also in eV. Species “M” in reaction (R21) represents a third-body.

Helium–oxygen chemistry (units are molecules-meter-electron volt)						
Index	Reaction	A	B	C	Threshold energy (eV)	References
(R1)	$\text{He} + e \rightarrow e + \text{He}^*$		BOLSIG+		19.8	34 and 35
(R2)	$\text{He} + e \rightarrow 2e + \text{He}^+$		BOLSIG+		24.6	34 and 35
(R3)	$e + \text{He}^* \rightarrow 2e + \text{He}^+$	4.661×10^{-16}	0.6	4.78	4.78	18
(R4)	$2\text{He}^* \rightarrow e + \text{He} + \text{He}^+$	4.5×10^{-16}	0	0	−15	18
(R5)	$e + \text{He}^* \rightarrow e + \text{He}$	1.099×10^{-17}	0.31	0	−19.8	18
(R6)	$e + \text{He}_2^* \rightarrow 2e + \text{He}_2^+$	1.268×10^{-18}	0.71	3.4	3.4	18
(R7)	$e + \text{He}_2^+ \rightarrow \text{He}^* + \text{He}$	5.386×10^{-13}	−0.5	0	0	18
(R8)	$\text{He}^* + 2\text{He} \rightarrow \text{He}_2^* + \text{He}$	1.3×10^{-45}	0	0	...	18
(R9)	$\text{He}^+ + 2\text{He} \rightarrow \text{He}_2^+ + \text{He}$	1.0×10^{-43}	0	0	...	18
(R10)	$e + \text{He}^+ \rightarrow \text{He}^*$	7.314×10^{-17}	−0.5	0	0	18
(R11)	$2e + \text{He}^+ \rightarrow e + \text{He}^*$	1.04×10^{-20}	−4.5	0	0	18
(R12)	$e + 2\text{O}_2 \rightarrow \text{O}_2 + \text{O}_2^-$	6.0×10^{-39}	−1.0	0	0	18
(R13)	$e + \text{O}_2 \rightarrow e + \text{O}_2(v3)$		BOLSIG+		0.57	34 and 35
(R14)	$e + \text{O}_2 \rightarrow e + \text{O}_2(v4)$		BOLSIG+		0.75	34 and 35
(R15)	$e + \text{O}_2 \rightarrow e + \text{O}_2(a1)$		BOLSIG+		0.977	34 and 35
(R16)	$e + \text{O}_2 \rightarrow e + \text{O}_2(b1)$		BOLSIG+		1.627	34 and 35
(R17)	$e + \text{O}_2 \rightarrow e + \text{O}_2(\text{exc})$		BOLSIG+		4.5	34 and 35
(R18)	$e + \text{O}_2 \rightarrow e + \text{O} + \text{O}$		BOLSIG+		6.0	34 and 35
(R19)	$e + \text{O}_2 \rightarrow e + \text{O} + \text{O}(^1\text{D})$		BOLSIG+		8.4	34 and 35
(R20)	$e + \text{O}_2 \rightarrow 2e + \text{O}_2^+$		BOLSIG+		12.06	34 and 35
(R21)	$\text{O}_2^- + \text{O}_2^+ + \text{M} \rightarrow 2\text{O}_2 + \text{M}$	3.12×10^{-31}	−2.5	0	...	18

electron collision with heavy species, the reaction rate coefficients were obtained using BOLSIG+, a Boltzmann equation solver.³⁴ The electron transport coefficients were also calculated using BOLSIG+. The cross-sections used in the calculation were obtained from Ref. 35. The transport coefficients for ions and metastables were obtained from Refs. 25 and 36. Photo-ionization was not considered in the model; following published works,^{15,16} a background pre-ionization was assumed, instead. According to Breden *et al.*,¹⁷ photo-ionization can affect the streamer (plasma bullet) propagation speed, but it is not needed to sustain the streamer. The wall destruction probability of He^* , He_2^* , He^+ , He_2^+ , O_2^- , and O_2^+ was set equal to unity, whereas the wall recombination probability of O-atoms was 0.02.³⁷ The system of Eqs. (4)–(7) and (13) was solved by a time-dependent solver in COMSOL.³⁰ Triangular finite elements were used with a finer grid in the region $r < 1$ mm and close to the substrate surface. The minimum mesh size was 0.01 mm. Nearly 12 000 elements were employed and the total number of degrees of freedom was $\sim 1\,000\,000$. Reducing the grid size to half of that of the base case, yielded profiles essentially identical to the base case, implying grid convergence.

A question can arise concerning the effect of rotational and vibrational states of molecular oxygen on the system behavior. A test simulation including several vibrational excitation channels of oxygen showed no significant effect of these processes on the plasma bullet dynamics. This may be due to the high electron temperatures in the system (see below) that favor high activation energy processes. Indeed, plasma bullet propagation is governed by electron-impact ionization of helium atoms and oxygen molecules.¹⁷

The neutral gas flow model and the plasma dynamics model were solved sequentially. This time, the splitting approach is valid because of the disparate time scales of the neutral gas flow and the plasma flow. In addition, the coupling between the neutral gas flow model and the plasma dynamics model is rather weak.^{18,27,28} First, the neutral gas flow model was solved to obtain the steady-state fluid velocity and concentration (He and O_2) profiles. These were in turn used as input to the plasma dynamics model to obtain the time-dependent charged and minority neutral species concentrations as well as the electric field profiles. This simulation method is similar to that reported by Naidis^{15,16} and Breden and Raja.¹⁸

III. RESULTS AND DISCUSSION

The base case parameter values used in the simulation were as follows: geometry as shown in Figure 1; pressure, 760 Torr; gas temperature, 300 K; applied voltage, +5 kV for 150 ns (including 10 ns rise time and 10 ns fall time); 5 mm gap between the tube exit and the substrate; and conductive (metal) substrate. The effect of a 3 mm gap, a 0.5 mm-thick insulating substrate having relative permittivity of 5 or 15, as well as the effect of system pressure (250–760 Torr) was investigated.

A. Steady state properties of the neutral gas

Figure 2 shows the helium mole fraction distribution for the base case as well as for a 3 mm gap. The helium mole fraction is essentially unity inside the tube. Back diffusion of oxygen into the tube is negligible since the corresponding

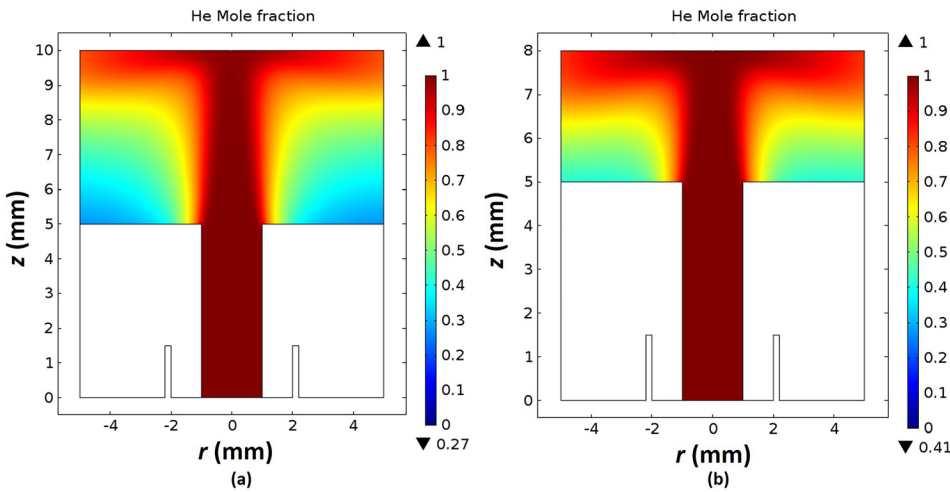


FIG. 2. Helium mole fraction profiles for (a) 5 mm gap between the tube exit and the substrate, and (b) 3 mm gap. Other parameters at their base case values.

Peclet number is $Pe = u L/D \sim 350 \gg 1$ where u is the average helium flow velocity in the tube, L is the tube length, and D is the diffusion coefficient of oxygen in helium. As the flow exits the tube, the helium mole fraction decreases in both the z - and r -direction, due to mixing (by convective diffusion) of the ambient oxygen with the helium gas. When the gas reaches the substrate, it flows radially outwards (stagnation point flow), which is similar to previous simulation results.¹⁸ As expected, in the 5 mm gap case, the pure helium core near the substrate location has smaller diameter, since oxygen mixing occurs for longer time, compared to the 3 mm gap. The mole fraction distribution of He in the He/O₂ mixture is critical for confining and guiding the plasma bullet. In fact, the radial extent of the bullet is confined to the region where the He mole fraction is above ~ 0.99 .¹⁵ The plasma cannot be sustained beyond a certain concentration of oxygen (a certain radial position) because the ionization rate coefficient vs. E/N (electric field to neutral gas density ratio) decreases sharply as the oxygen mole fraction in the He-O₂ mixture increases.¹⁵ The diameter of the He core of the jet shrinks as a function of distance from the tube exit, then expands upon striking the substrate (see below). The constriction of the diameter of the He core of the jet is not as pronounced in the 3 mm compared to the 5 mm gap.

B. Conductive substrate

Although it appears continuous to the naked eye, the discharge is actually composed of fast ionization waves (streamers, also called plasma bullets) traveling at supersonic speeds in the dielectric tube and in the gap between the tube exit and the substrate.⁷ The spatio-temporal distribution of the ionization rate is shown in Fig. 3 for conductive (a) and insulating (b) substrates. Over a period of the applied voltage pulse, the discharge starts as a surface ionization wave adjacent to the containing tube wall. A plasma bullet then forms that is launched in the gap at $t \sim 22$ ns, and propagates towards the substrate. The bullet starts as a donut-shaped structure (ionization peaks off axis), but the “hole” fills in as the bullet travels further downstream, resulting in peak ionization on the axis. The average propagation speed of the plasma bullet in the gap is $\sim 2 \times 10^5$ m/s, in the range of values reported by other investigators (Ref. 7 and references therein). Upon striking a metal (conductive) substrate (Fig. 3(a)) at $t \sim 45$ ns, the plasma bullet forms a conductive channel to the substrate. Eventually ionization is suppressed when the He mole fraction drops below ~ 0.99 .

Previous computational studies (Naidis *et al.*,¹⁵ Breden *et al.*,³⁸ Boeuf *et al.*,³⁹ and Lu *et al.*²⁶) have provided insights into the structure of the plasma bullet emerging in air ambient. The main difference in the structure of the

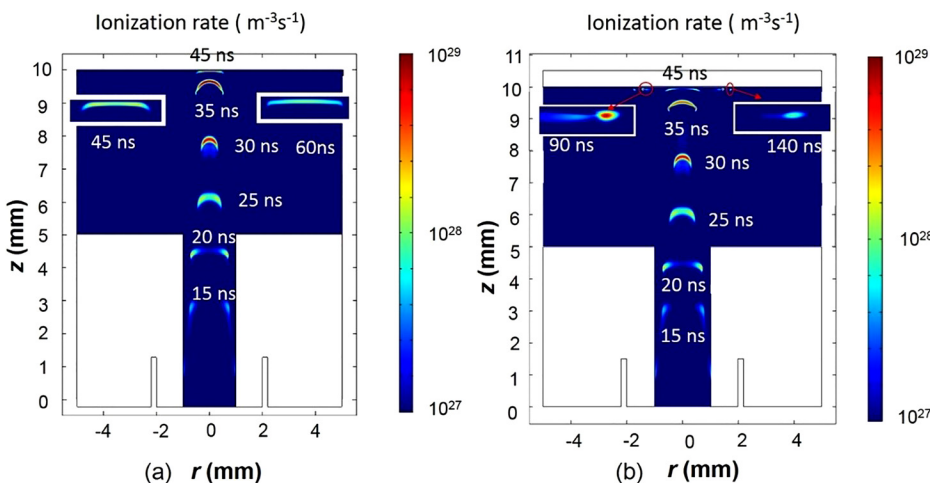


FIG. 3. Spatiotemporal evolution of the total ionization rate (including reactions (R2), (R3), (R4), (R6), and (R20), see Table III) for conductive (a), and insulating (b), substrates. The plasma bullet is shown at different times during a voltage pulse. Rectangular insets show expanded scale of the plasma bullet near the substrate at 45 and 60 ns for the conductive substrate and 90 and 140 ns, for the insulating substrate. For $t=90$ and 140 ns, the ionization rate is multiplied by 10 for better visualization.

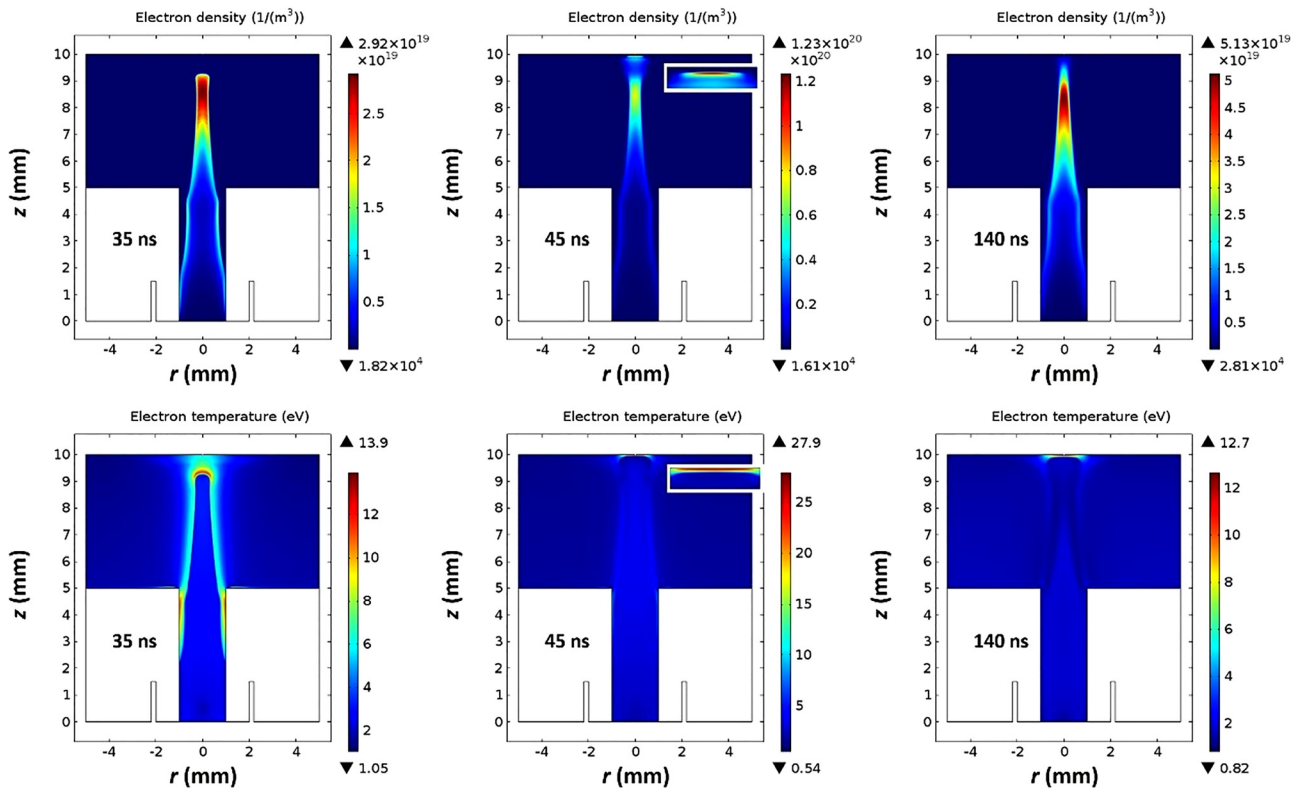


FIG. 4. Spatial profiles of electron density and electron temperature at $t=35$ (left panels), 45 (middle panels), and 140 ns (right panels). Parameters were at their base case values. Rectangular insets show expanded scale of electron density and electron temperature near the substrate at $t=45$ ns.

plasma bullet between previous studies and our work is that the radial extends and the spatial evolution of the ionization profile of our plasma bullet follows the evolution of the helium core of Fig. 2, i.e., the bullet constricts as it propagates downstream, only to expand upon hitting the substrate.

Figure 4 shows the spatial distribution of electron density and electron temperature at $t=35, 45,$ and 140 ns during a pulse, for a conductive (metal) substrate. When the power is applied, the discharge is ignited at the downstream edge of the high voltage ring electrode. A surface discharge forms near the tubular wall, and the maximum electron temperature ($T_e = 10.4$ eV) is also near the tube wall. At $t=22$ ns, the plasma bullet exits the dielectric tube and propagates axially towards the substrate. At time $t=35$ ns, the bullet reaches an axial position of 4.2 mm from the tube exit (see also Fig. 3). The electron density is initially donut-shaped, but the “hole” fills-in further downstream, mimicking the behavior of the plasma bullet. At about $t=45$ ns, the bullet impacts the

surface, creating a peak in the electron density (and electron temperature) near the surface. From 45 ns to 140 ns, the discharge “connects” to the substrate via a rather concentrated spot. The electrons are quite hot near the surface even at $t=140$ ns due to the high electric field near the conductive substrate.

Figure 5 shows the axial electric field and the electron temperature, along the axis of symmetry ($r=0$), for different times during a pulse. Axial position $z=6$ mm is 1 mm downstream from the tube exit, and $z=10$ mm signifies the substrate surface. Insets show an expanded view ($z=9.5-10$ mm) near the substrate. Since the rate of electron-impact reactions is a strong function of T_e , or reduced electric field E/N , it is important to understand the dependence of these variables on system parameters. At any given time, the spatial profiles of the electric field and electron temperature are very similar (excluding the region near the substrate surface), implying that the local field approximation may be applicable. In the local

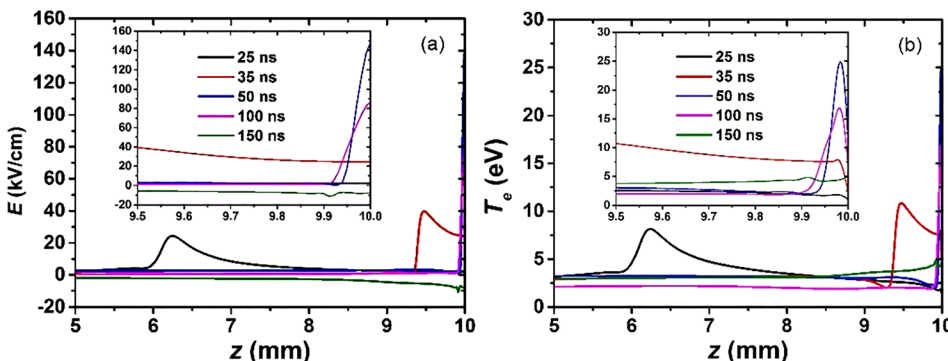


FIG. 5. Axial electric field (a) and electron temperature (b) along the axis of symmetry for several times during a pulse. Parameters were at their base case values.

field approximation, the electron energy equation (Eq. (6)) is not used. Instead, the electron energy is assumed to depend on the local value of the reduced field E/N , where the electric field E is calculated by the Poisson equation (Eq. (7)).^{15,16} The relationship between E/N and average electron energy (or equivalent electron temperature) can be found by solving the Boltzmann equation. The region next to the substrate is non-local, e.g., the peak E is at the substrate but the peak T_e is a bit removed from the substrate.

Figure 5 also shows that the peak electric field and electron temperature are found at the plasma bullet head. As the bullet approaches the conductive substrate, the axial electric field and electron temperature at the head both increase. At $t = 50$ ns, the peak electric field and electron temperature are 148 kV/cm and 25 eV, respectively. After the bullet strikes the substrate, the electric field and electron temperature decrease rapidly. The electric field switches signs from positive to negative near the end ($t = 150$ ns) of the pulse. This is due to residual charges on the inner surface of the dielectric tube,⁴⁰ which now plays the role of cathode, while the substrate switches roles from cathode to anode. This reverse electric field accelerates electrons towards the substrate, igniting a “backward” discharge, albeit for only a short time. Electron heating by this field is seen close to the substrate in Fig. 5 (green line).

Figure 6 shows the calculated spatial distribution of species densities at $t = 110$ ns. He^+ is generated mainly in the streamer head by electron impact ionization of He and at a lower rate in the plasma channel upstream of the head by reaction (R4). The peak value of He^+ density is $5.3 \times 10^{18} \text{ m}^{-3}$. Since He^+ is quickly turned into He_2^+ by reaction (R9), the density of He_2^+ has a similar spatial profile as He^+ . The He_2^+

density is one order of magnitude higher than the He^+ density. Metastable He^* (peak density $9.36 \times 10^{20} \text{ m}^{-3}$) has the same spatial profile as the excimer He_2^* (peak density $4.27 \times 10^{19} \text{ m}^{-3}$). The dominant ion is O_2^+ , albeit its density is a bit lower than the sum of the He^+ and He_2^+ densities. The peak O-atom density is $2.5 \times 10^{21} \text{ m}^{-3}$, commensurate with measurements,¹⁴ implying that the plasma jet is a good source of reactive O radicals.

A significant advantage of the plasma jet is its ability to deliver high fluxes of reactive species to a surface under treatment. Figs. 7(a) and 7(b) show the radial distribution of the flux of neutrals and ions onto a conductive substrate at time $t = 110$ ns. The fluxes peak on the axis of symmetry, and plasma-surface interaction occurs primarily within only a 1 mm radius. The flux of neutral species is lower than the positive ion flux, since the only driving force for neutrals is diffusion, while ions are also under the influence of the electric field. The He^* and O fluxes are dominant among the neutral species. For positive ions, the He^+ flux dominates, due to the high mobility of these ions. Negative ions cannot strike the substrate as long as the sheath repels them. However, near the end of the pulse, the electric field reverses and negative ions (as well as accelerated electrons) can strike the surface. The radial flux distribution of O_2^- at $t = 150$ ns is shown in Fig. 7(c). O_2^- has a similar flux distribution to that of other species, with a peak flux $\sim 4.6 \times 10^{19} \text{ m}^{-2} \text{ s}^{-1}$.

1. Effect of gap size

In this subsection, the effect of decreasing the gap between the tube exit and the substrate surface from 5 mm to

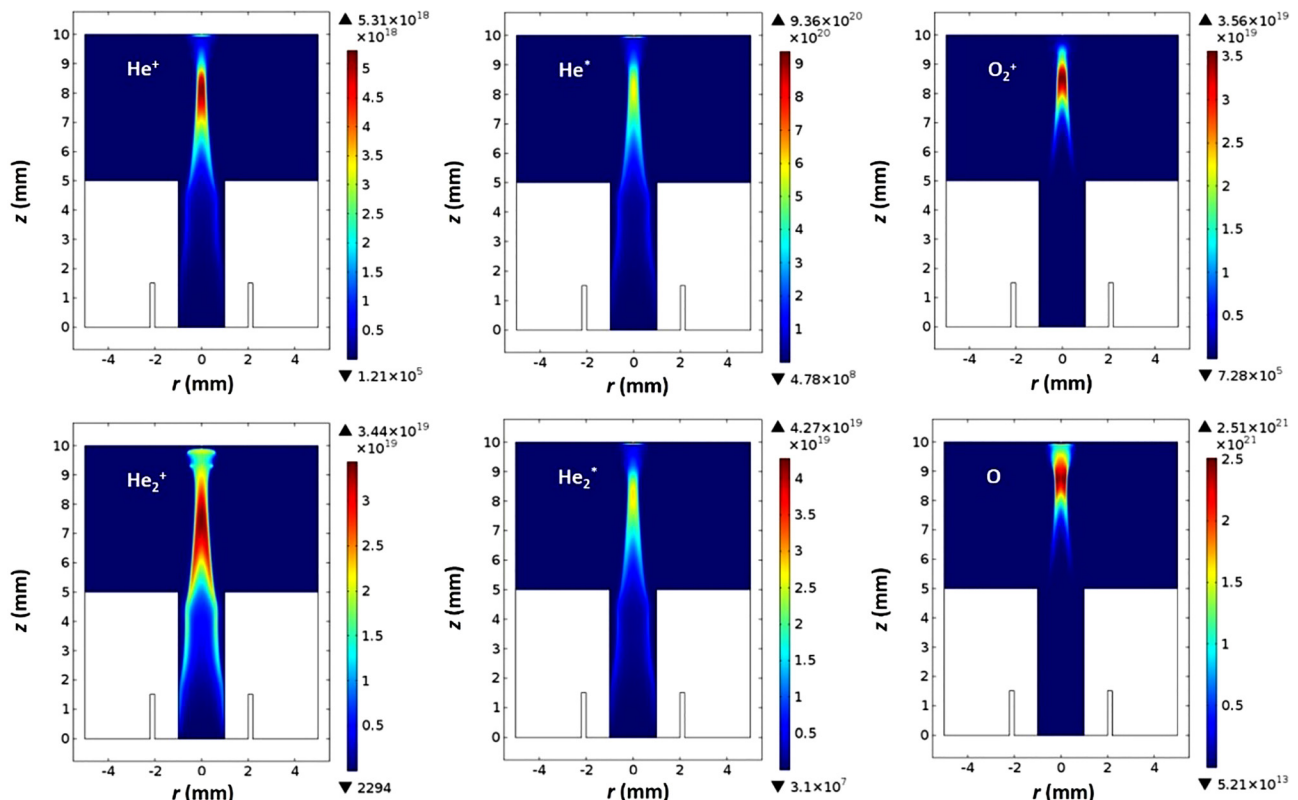


FIG. 6. Spatial distribution of species densities at 110 ns. Parameters were at their base case values.

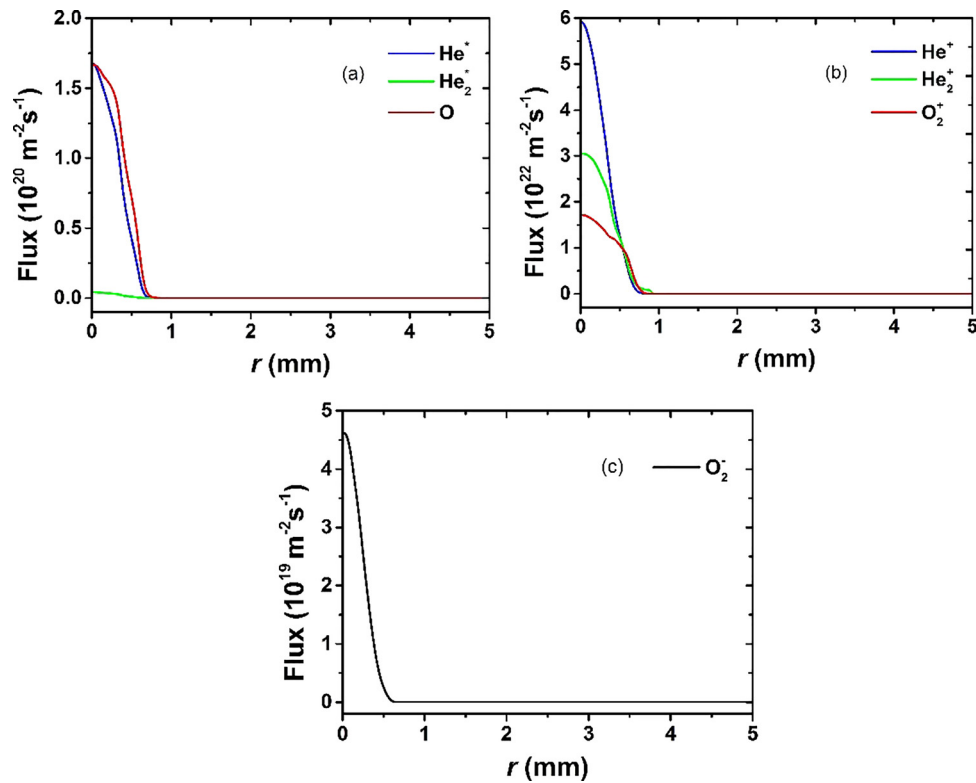


FIG. 7. Flux of (a) neutrals at $t = 110$ ns, (b) positive ions at $t = 110$ ns, and (c) O_2^- negative ions at $t = 150$ ns on the conductive substrate. Parameters were at their base case values.

3 mm is examined. All other parameters were kept at their base case values. The gas flow model yielded the helium mole fraction corresponding to this geometry as shown in Figure 2(b). A smaller gap results in thicker pure helium core, which extends to a larger radial distance along the substrate.

The spatial distributions of electron density and electron temperature at $t = 35$, 45, and 140 ns are shown in Fig. 8. Discharge initiation and propagation in the dielectric tube is hardly affected by the gap size. As the discharge is launched into the helium–oxygen mixing layer, however, the plasma jet diameter is larger in the shorter gap, because the exposure time of the helium jet to the ambient oxygen is shorter, resulting in shorter penetration depth of the oxygen into the helium jet. This is also confirmed by experimental observations.²⁰ In addition, the smaller gap results in a shorter propagation time of the streamer from the tube exit to the substrate surface. At about $t = 35$ ns, the plasma bullet impacts the surface, creating a peak in the electron density (and electron temperature) near the surface. The peak electron temperature is 27.9 eV.

After impact, both electron temperature and density near the surface decrease, as electrons flow from ground to neutralize the positive ion flux. Electrons cannot strike the substrate in the presence of a positive electric field. The electron density is kept some distance away from the substrate as shown in Fig. 8 at $t = 140$ ns. A cathode sheath is present, and the electron temperature in the sheath is about 6 eV.

A comparison of the flux distribution of neutral species and positive ions, on a conductive surface, at time $t = 110$ ns, for the two gaps is given in Fig. 9. In both cases, the fluxes peak on the axis of symmetry and gradually decrease away

from the axis. For the 3 mm gap case, the footprint of the plasma–surface interaction appears larger than that of the 5 mm case. Decreasing the distance between the tube exit and the substrate is therefore desirable to maximize the plasma–surface interaction area. However, the peak value of the species flux (especially for O and O_2^+) decreases as the gap is decreased. The decrease of the O and O_2^+ fluxes is mainly due to the lower oxygen mole fraction in the diffusion layer in the shorter gap case (compare Figures 2(a) and 2(b)). Also, the ionization front residence time is shorter for the smaller gap, resulting in less ionization and dissociation.

2. Effect of gas pressure

Neglecting buoyancy effects, the fluid mechanics and mass transfer in a laminar jet are controlled by the Reynolds number ($\text{Re} = uL/\nu$) and the Peclet number ($\text{Pe} = uL/D$). Here, u and L are characteristic gas velocity and length scale, respectively, ν is kinematic viscosity, and D is diffusivity. As pressure decreases, the gas flow velocity increases

TABLE IV. Base case parameter values and range studied.

Parameter	Base case value	Range investigated
Pressure	760 Torr	250, 500, and 760 Torr
Applied voltage and duration	5 kV, 150 ns	
Gap between tube exit and substrate	5 mm	3, 5 mm
Substrate	Conductor	Insulator
Relative permittivity of insulating substrate	5	5, 15

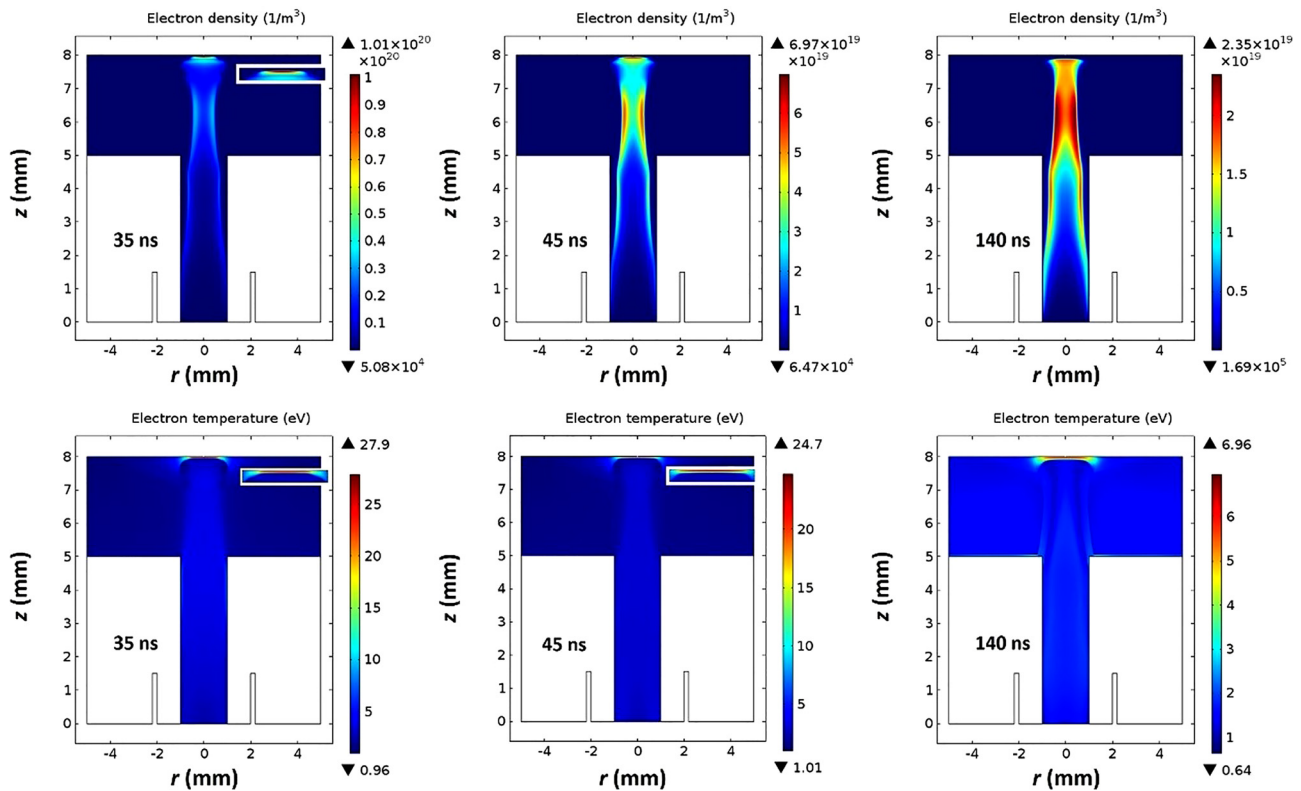


FIG. 8. Spatial profiles of electron density and electron temperature at $t=35$ (left panels), 45 (middle panels), and 140 ns (right panels). Parameters were at their base case values except that the gap between the tube exit and the substrate was 3 mm. Rectangular insets show expanded scale of electron density (at $t=35$ ns), and electron temperature (at $t=35$ and 45 ns) near the substrate.

proportionally, but so do the diffusion coefficient and kinematic viscosity. Thus, the Re and Pe numbers remain unchanged, and the results of Fig. 2 (in terms of mole fractions) are valid at the reduced pressures as well. When varying pressure, all other parameters were kept at their base case values (Table IV). The spatial distributions of electron density and electron temperature at $t=20, 35, 140$ ns for a gas pressure of 500 Torr are shown in Fig. 10. When compared to the corresponding Fig. 4 for 760 Torr, one observes that the discharge is initiated earlier at the reduced pressure. This may be attributed to the breakdown voltage of helium decreasing by reducing pressure (right branch of the Paschen curve). Also, the average propagation velocity of the plasma bullet increases from 2×10^5 m/s at 760 Torr to 5×10^5 m/s when pressure is reduced to 500 Torr. A lower pressure results in higher electron temperature in the head of the plasma bullet, leading to a higher propagation velocity.

Fig. 11 shows the radial flux distribution of neutral species and positive ions on the conductor surface, at time $t=110$ ns for $p=500$ and 250 Torr. This is to be compared to Fig. 7 at 760 Torr. In going from 760 to 250 Torr, the plasma–surface interaction area increases from ~ 1 mm to ~ 2 mm radius, but the peak value of the species flux decreases. The O flux dominates among the minority neutral species. At 500 Torr, the peak of the O-atom flux is near the axis, but at 250 Torr, the peak of O flux is ~ 1 mm off the axis.

C. Insulating substrate

In this subsection, the effect of insulating substrate is studied by placing a 0.5 mm-thick dielectric layer (relative permittivity of 5) on a grounded conductor. All other parameters were kept constant. The plasma bullet evolution with a dielectric substrate (Fig. 3(b)) is similar to that with a

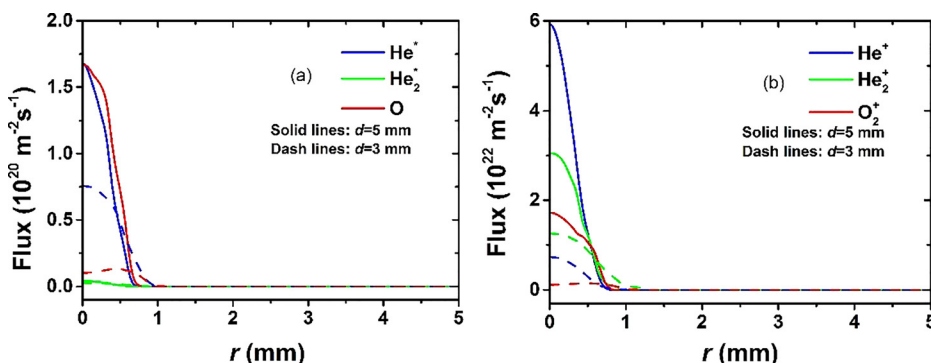


FIG. 9. Flux of (a) neutrals and (b) positive ions onto a conductive substrate at $t=110$ ns, for 5 mm and 3 mm gap between the jet exit and the substrate surface.

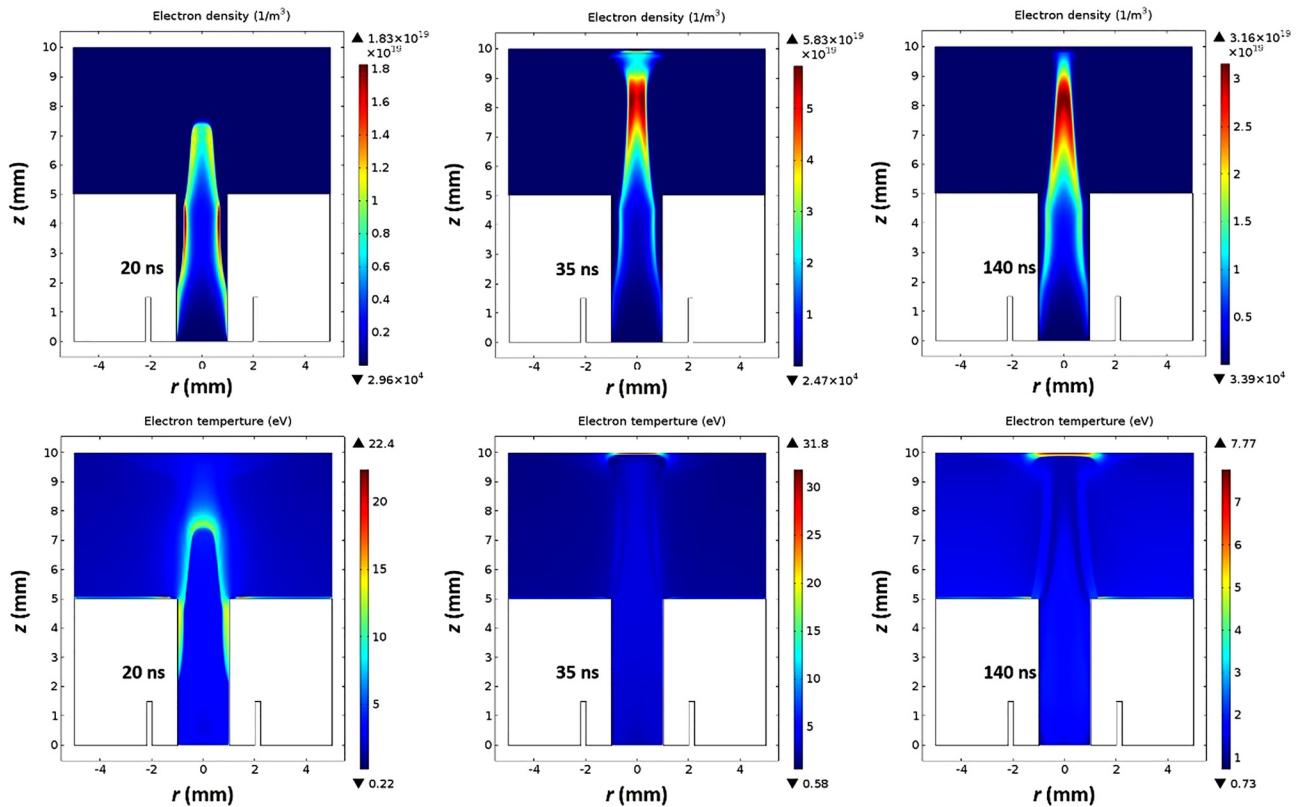


FIG. 10. Spatial profiles of electron density and electron temperature at $t=20$ (left panels), 35 (middle panels), and 140 ns (right panels). Parameters were at their base case values except that the gas pressure was 500 Torr.

conductive substrate up to $t \sim 35$ ns, when the plasma bullet is near the surface. Upon striking the insulating surface, the streamer spreads radially outwards while ionization and dissociation reactions continue to occur. Eventually, this radially directed surface ionization wave, produced by radial electric fields due to substrate charging,¹⁹ is suppressed as in the case of conductive substrate.

Fig. 12 shows the distribution of electron density and electron temperature at $t=35, 60,$ and 140 ns. The dynamics of discharge ignition and propagation inside the dielectric tube, and across most of the gap outside the tube, is hardly affected by the electrical properties of the substrate. After the plasma bullet contacts the substrate, however, charge-up of the insulator causes the plasma bullet to spread along the dielectric surface to a radius of 2 mm. This result is in agreement with Ref. 18. Note that when the substrate is conductive, the discharge “connects” to the substrate via a

rather concentrated spot instead of spreading out. This is in agreement with the experimental observations of Ref. 28. During the radial propagation of a surface ionization front (60 ns–140 ns), the electron temperature in the ionization front decreases from 16.7 eV to 8.6 eV.

To further investigate the interaction of the plasma bullet with an insulating substrate, the axial electric field and electron temperature along the axis of symmetry are shown in Fig. 13, for different times during a pulse. As in the case of Fig. 5, the peak electric field and electron temperature are located at the bullet head. As the bullet approaches the insulator surface, the maximum axial electric field and electron temperature both increase. The bullet impacts the insulator surface at $t=43$ ns. As the bullet head strikes, a charge is deposited on the surface. The accumulated surface charge can create a negative self-induced potential in the gap and a decrease of the electric field. The higher the accumulated surface charge, the

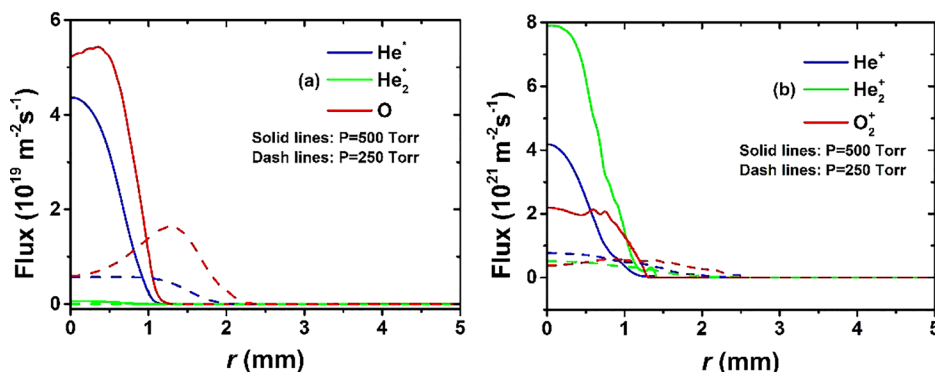


FIG. 11. Flux of (a) neutrals and (b) positive ions onto a conductive substrate, at $t=110$ ns, for different gas pressures.

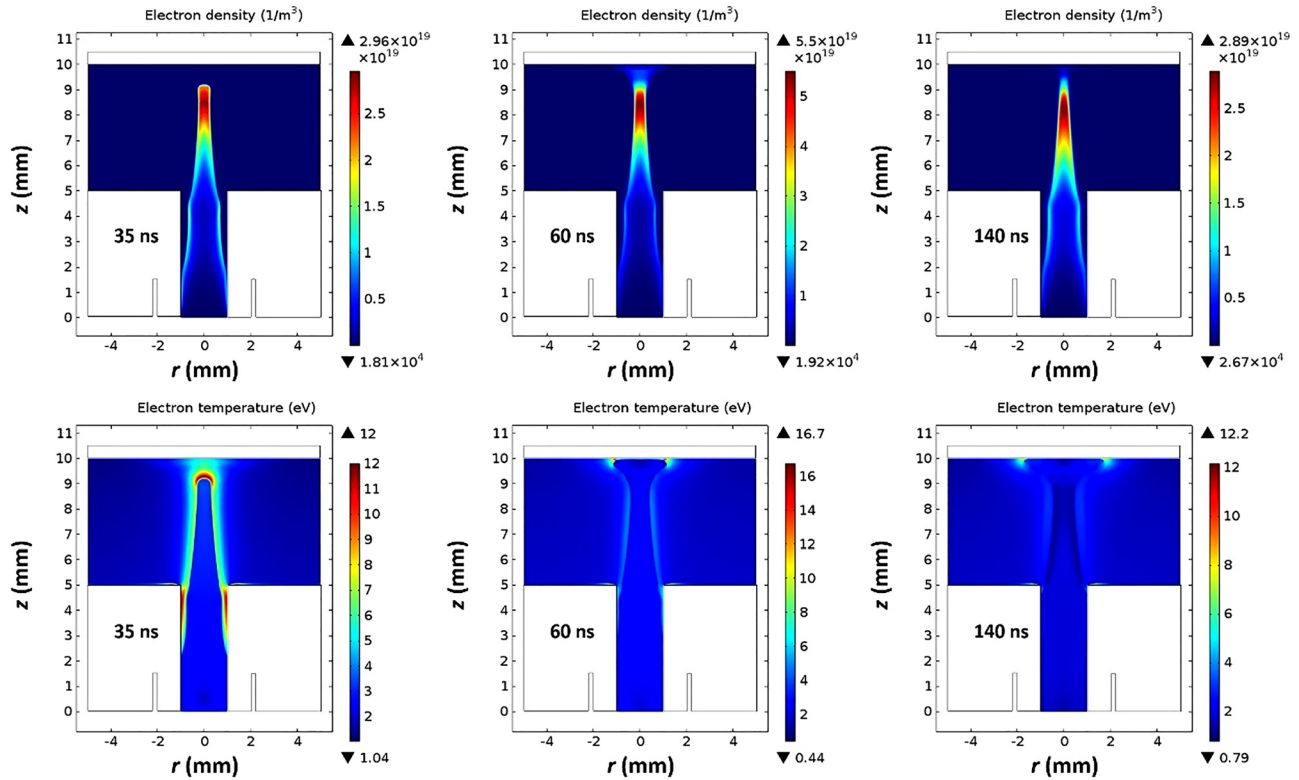


FIG. 12. Spatial distributions of the electron density and electron temperature at $t = 35$ (left panels), 60 (middle panels), and 140 ns (right panels) for 5 mm gap, and 0.5 mm-thick insulating surface with a permittivity of $\epsilon_r = 5$.

weaker the net electric field. Thus, for time $t = 50$ ns, the peak electric field and electron temperature on axis close to the wall are only 30 kV/cm and 8 eV, respectively, much lower than the case with a conductive substrate. As mentioned above, during the voltage decay of the pulse ($t = 140$ – 150 ns), a secondary discharge is induced by the charges deposited on the surface of the insulator, much like a dielectric barrier discharge. During this time period, the electron temperature increases as electrons are accelerated towards the surface.

1. Effect of relative permittivity

Figure 14 shows the radial flux distributions of neutral species and positive ions on the insulator surface, at time $t = 110$ ns for $\epsilon_r = 5$ and $\epsilon_r = 15$. In both cases, the peak of

species flux is some distance from the axis of symmetry (hollow profiles). Chemistry occurring during the radial propagation of a surface ionization front in the case of the insulating substrate contributes to the off-axis maxima. The O-atoms dominate the neutral species flux while He^+ and O_2^+ dominate the positive ion flux. For $\epsilon_r = 5$, the “footprint” of the plasma–surface interaction appears larger compared to $\epsilon_r = 15$. This is due to increasing bullet speed with decreasing ϵ_r as the ionization front propagates along the dielectric substrate. As the discharge spreads to larger radii on the surface, its intensity decreases due to progressively higher oxygen mole fraction. In addition, as shown in Figure 14, $\epsilon_r = 5$ yields lower species fluxes compared to $\epsilon_r = 15$. This is because decreasing ϵ_r results in lower electric field over the dielectric surface after the bullet impacts the surface.^{41,42}

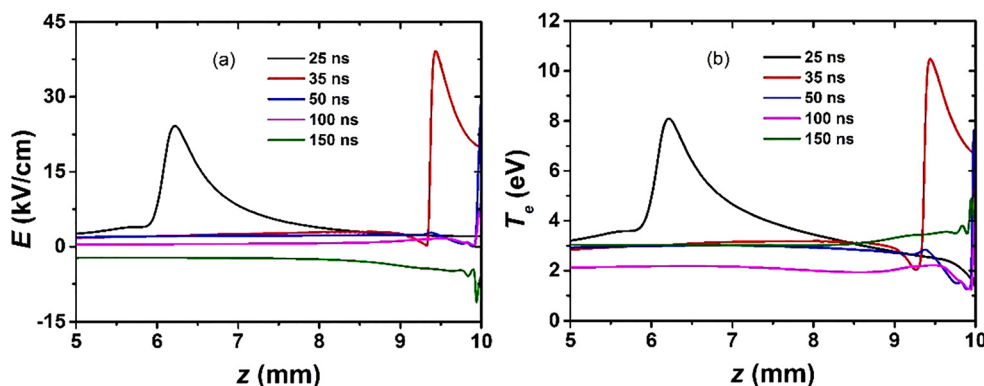


FIG. 13. Axial profiles of electric field (a) and electron temperature (b) on the axis of symmetry ($r = 0$) for several times during a pulse, for 5 mm gap, and 0.5 mm-thick insulating surface with a permittivity of $\epsilon_r = 5$.

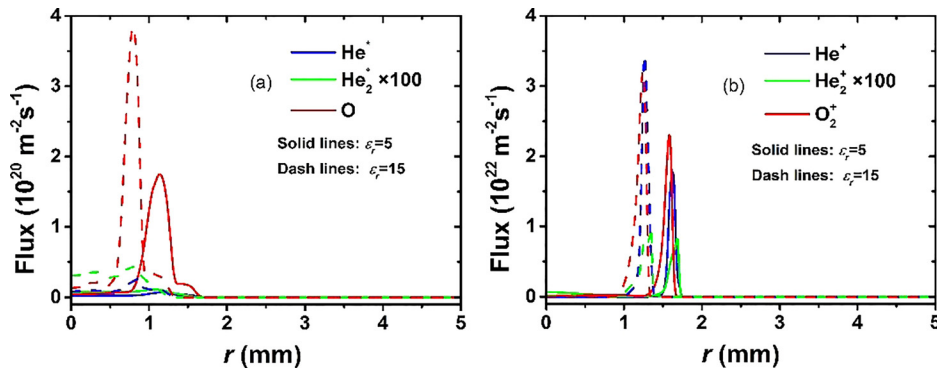


FIG. 14. Flux of (a) neutrals and (b) positively charged ions onto a 0.5 mm thick insulating surface at $t = 110$ ns for $\epsilon_r = 5$ and $\epsilon_r = 15$.

2. Effect of gas pressure

As discussed above, the plasma bullet evolution with a dielectric substrate is similar to that with a conductive substrate except when the bullet is near the surface. Therefore, emphasis was placed on the influence of pressure on the distributions of species flux onto the insulator surface. Figure 15 shows the radial flux distributions of neutral species and positive ions on the insulator surface, at time $t = 110$ ns for $p = 500$ Torr and $p = 250$ Torr. Lowering the pressure from atmospheric to 250 Torr, the plasma–surface interaction radius increases from about 1 mm to 3 mm, but the peak value of the species flux (except O_2^+) decreases. The O-atoms dominate the neutral species flux at 500 Torr, and the peaks of the helium excited state (He^* and He_2^*) fluxes move toward the axis as the pressure decreases, eventually resulting in peak helium metastable on axis at pressure 250 Torr. For both pressures, the peak of positive ion flux is some distance from the axis of symmetry (hollow profiles). The dominant positive ion flux to the surface changes from He_2^+ to O_2^+ when the pressure decreases from 500 to 250 Torr.

IV. SUMMARY AND CONCLUSIONS

A computational investigation of the plasma bullet resulting from a cold plasma jet in helium, flowing inside a dielectric tube and then emerging in oxygen ambient at high pressures (250–760 Torr) was conducted, based on a two-dimensional fluid model. Neutral gas flow and mass transport as well as plasma dynamics were included in the model. Emphasis was placed on the interaction of the plasma bullet with a substrate, for different electrical properties of the substrate (e.g., conductor vs. insulator). The effect of gap between the tube exit and the substrate, relative permittivity of the insulating substrate and gas pressure, on the discharge

properties was also studied. The spatiotemporal evolution of the discharge during a 150 ns, +5 kV trapezoidal pulse (10 ns each for rise and fall times) applied to a ring electrode encircling the dielectric tube was analyzed. The discharge was initiated at the downstream edge of the ring electrode. Inside the dielectric tube, the discharge started as a surface wave along the wall of the tube. A plasma bullet (streamer) was then formed that was launched in the free space between the tube end and the substrate. The bullet was donut-shaped (ionization peaked off axis) upon exiting the tube, but ionization peaked on axis further downstream.

Upon impact on a metal (conductive) substrate, the bullet established a conductive channel to the substrate. The species flux to a conductive substrate peaked on axis and decreased rapidly in the radial direction along the surface. The peak positive ion flux was $\sim 10^{22} \text{ m}^{-2} \text{ s}^{-1}$. The dominant positive ion and neutral species fluxes to the surface were He^+ , He^* , and O, respectively. When the gap between the tube exit and the substrate surface was reduced from 5 mm to 3 mm, the bullet–surface interaction area increased, while the peak species flux decreased, mainly for O and O_2^+ .

For an electrically insulating substrate, the discharge spread along the radius of the dielectric surface. Species continued to be produced by a surface ionization wave as it propagated along the radius. As a consequence, the species flux peaked off-axis. The dominant ion fluxes were those of He^+ and O_2^+ , whereas the O-atom flux was dominant among the neutral species. The plasma–surface interaction area increased when the relative permittivity of the insulator decreased.

The propagation velocity of the plasma bullet and the area of direct interaction between the bullet and the substrate both increased by reducing pressure. For insulating substrate, the dominant positive ion flux to the surface changed from

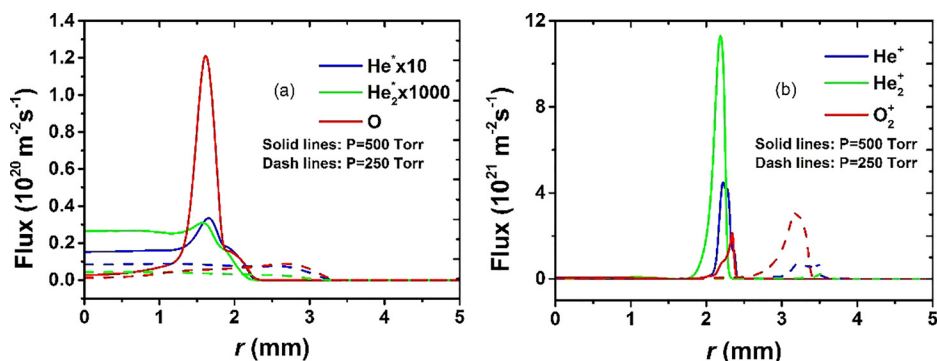


FIG. 15. Flux of (a) neutrals and (b) positive ions onto a 0.5 mm thick insulating surface at $t = 110$ ns, for two different gas pressures.

He₂⁺ to O₂⁺ when the pressure decreased from 500 Torr to 250 Torr. Lower pressure favored larger radial displacement of the peak of the positive ion fluxes. A reverse electric field developed during the late stages of the ramp-down of the pulse, which accelerated electrons forming a brief backward discharge.

ACKNOWLEDGMENTS

This work was supported by the Department of Energy, Office of Fusion Energy Science, Contract No. DE-SC0001939. Wen Yan is grateful to the National Natural Science Foundation of China for a study abroad grant.

- ¹M. Laroussi and T. Akan, *Plasma Processes Polym.* **4**, 777 (2007).
- ²M. G. Kong, G. Kroesen, G. Morfill, T. Nosenko, T. Shimizu, J. Van Dijk, and J. L. Zimmermann, *New J. Phys.* **11**, 115012 (2009).
- ³J. Schlegel, J. Körtzner, and V. Boxhammer, *Clin. Plasma Med.* **1**, 2 (2013).
- ⁴X. Zhang and S. Ptasinska, *J. Phys. D: Appl. Phys.* **47**, 145202 (2014).
- ⁵D. B. Graves, *Phys. Plasmas* **21**, 080901 (2014).
- ⁶H. Paetzelt, G. Böhm, and T. Arnold, *Plasma Sources Sci. Technol.* **24**, 025002 (2015).
- ⁷X. Lu, M. Laroussi, and V. Puech, *Plasma Sources Sci. Technol.* **21**, 034005 (2012).
- ⁸X. Lu, G. V. Naidis, M. Laroussi, and K. Ostrikov, *Phys. Rep.* **540**, 123 (2014).
- ⁹M. Teschke, J. Kedzierski, E. G. Finantu-Dinu, D. Korzec, and J. Engemann, *IEEE Trans. Plasma Sci.* **33**, 310 (2005).
- ¹⁰X. Lu and M. Laroussi, *J. Appl. Phys.* **100**, 063302 (2006).
- ¹¹N. Mericam-Bourdet, M. Laroussi, A. Begum, and E. Karakas, *J. Phys. D: Appl. Phys.* **42**, 055207 (2009).
- ¹²Y. Sakiyama, D. B. Graves, J. Jarrige, and M. Laroussi, *Appl. Phys. Lett.* **96**, 041501 (2010).
- ¹³S. Park, W. Choe, H. Kim, and J. Y. Park, *Plasma Sources Sci. Technol.* **24**, 034003 (2015).
- ¹⁴J. B. Schmidt, B. L. Sands, W. D. Kulatilaka, S. Roy, J. Scofield, and J. R. Gord, *Plasma Sources Sci. Technol.* **24**, 032004 (2015).
- ¹⁵G. V. Naidis, *J. Phys. D: Appl. Phys.* **44**, 215203 (2011).
- ¹⁶G. V. Naidis, *IEEE Trans. Plasma Sci.* **43**, 733 (2015).
- ¹⁷D. Breden, K. Miki, and L. L. Raja, *Plasma Sources Sci. Technol.* **21**, 034011 (2012).
- ¹⁸D. Breden and L. L. Raja, *Plasma Sources Sci. Technol.* **23**, 065020 (2014).
- ¹⁹S. A. Norberg, E. Johnsen, and M. J. Kushner, *J. Appl. Phys.* **118**, 013301 (2015).
- ²⁰Y. Xian, P. Zhang, X. Pei, and X. Lu, *IEEE Trans. Plasma Sci.* **42**, 2448 (2014).
- ²¹A. Schmidt-Bleker, S. A. Norberg, J. Winter, E. Johnsen, S. Reuter, K. D. Weltmann, and M. J. Kushner, *Plasma Sources Sci. Technol.* **24**, 035022 (2015).
- ²²J. Winter, J. S. Sousa, N. Sadeghi, A. Schmidt-Bleker, S. Reuter, and V. Puech, *Plasma Sources Sci. Technol.* **24**, 025015 (2015).
- ²³D. X. Liu, M. Z. Rong, X. H. Wang, F. Iza, M. G. Kong, and P. Bruggeman, *Plasma Processes Polym.* **7**, 846 (2010).
- ²⁴G. Y. Park, Y. J. Hong, H. W. Lee, J. Y. Sim, and J. K. Lee, *Plasma Processes Polym.* **7**, 281 (2010).
- ²⁵J. He and Y. T. Zhang, *Plasma Processes Polym.* **9**, 919 (2012).
- ²⁶X. Y. Liu, X. K. Pei, X. P. Lu, and D. W. Liu, *Plasma Sources Sci. Technol.* **23**, 035007 (2014).
- ²⁷X. Lu, Z. Jiang, Q. Xiong, Z. Tang, and Y. Pan, *Appl. Phys. Lett.* **92**, 151504 (2008).
- ²⁸J. L. Walsh, J. J. Shi, and M. G. Kong, *Appl. Phys. Lett.* **88**, 171501 (2006).
- ²⁹X. Shao, Z. Chang, H. Mu, W. Liao, and G. Zhang, *IEEE Trans. Plasma Sci.* **41**, 899 (2013).
- ³⁰COMSOL 5.0 (COMSOL, Burlington, MA, 2014).
- ³¹W. Yan, F. Liu, C. Sang, and D. Wang, *Phys. Plasmas* **21**, 063505 (2014).
- ³²W. Yan, F. Liu, C. Sang, and D. Wang, *Phys. Plasmas* **21**, 013504 (2014).
- ³³Y. Sakiyama and D. B. Graves, *Plasma Sources Sci. Technol.* **18**, 025022 (2009).
- ³⁴G. Hagelaar and L. Pitchford, *Plasma Sources Sci. Technol.* **14**, 722 (2005).
- ³⁵See http://www.lxcat.laplace.univ-tlse.fr/cross_sec_download.php for cross section data.
- ³⁶Q. Wang, D. J. Economou, and V. M. Donnelly, *J. Appl. Phys.* **100**, 023301 (2006).
- ³⁷D. S. Stafford and M. J. Kushner, *J. Appl. Phys.* **96**, 2451 (2004).
- ³⁸D. Breden, K. Miki, and L. L. Raja, *Appl. Phys. Lett.* **99**, 111501 (2011).
- ³⁹J. P. Boeuf, L. L. Yang, and L. C. Pitchford, *J. Phys. D: Appl. Phys.* **46**, 015201 (2013).
- ⁴⁰S. Hübner, S. Hofmann, E. M. van Veldhuizen, and P. J. Bruggeman, *Plasma Sources Sci. Technol.* **22**, 065011 (2013).
- ⁴¹F. Pechereau, J. Jánký, and A. Bourdon, *Plasma Sources Sci. Technol.* **21**, 055011 (2012).
- ⁴²N. Y. Babaeva and M. J. Kushner, *Plasma Sources Sci. Technol.* **20**, 035017 (2011).